Article

The Interplay between ESIPT and TADF for the 2,2′-Bipyridine-3,3′-diol: A Theoretical Reconsideration

Xin Zhao, Lixia Zhu, Qi Li, Hang Yin * and Ying Shi *

Institute of Atomic and Molecular Physics, Jilin University, Changchun 130012, China
* Correspondence: yinhang@jlu.edu.cn (H.Y.); shi_ying@jlu.edu.cn (Y.S.)

Abstract: Organic molecules with excited-state intramolecular proton transfer (ESIPT) and thermally activated delayed fluorescence (TADF) properties have great potential for realizing efficient organic light-emitting diodes (OLEDs). Furthermore, 2,2′-bipyridine-3,3′-diol (BP(OH)$_2$) is a typical molecule with ESIPT and TADF properties. Previously, the double ESIPT state was proved to be a luminescent state, and the T$_2$ state plays a dominant role in TADF for the molecule. Nevertheless, whether BP(OH)$_2$ undergoes a double or single ESIPT process is controversial. Since different ESIPT channels will bring different TADF mechanisms, the previously proposed TADF mechanism based on the double ESIPT structure for BP(OH)$_2$ needs to be reconsidered. Herein, reduced density gradient, potential energy surface, IR spectra and exited-state hydrogen-bond dynamics computations confirm that BP(OH)$_2$ undergoes the barrierless single ESIPT process rather than the double ESIPT process with a barrier. Moreover, based on the single ESIPT structure, we calculated spin-orbit coupling matrix elements, nonradiative rates and electron-hole distributions. These results disclose that the T$_3$ state plays a predominant role in TADF. Our investigation provides a better understanding on the TADF mechanism in hydrogen-bonded molecular systems and the interaction between ESIPT and TADF, which further provides a reference for developing efficient OLEDs.

Keywords: excited-state intramolecular proton transfer; thermally activated delayed fluorescence; spin-orbit coupling; hydrogen-bond dynamics; electron-hole distribution

1. Introduction

Organic molecules with thermally activated delayed fluorescence (TADF) properties have aroused extensive attention due to their significant applications in organic light-emitting diodes (OLEDs) [1–5]. These applications are attributed to their high utilization of both singlet and triplet excitons. For conventional fluorescent OLEDs, only 25% singlet excitons are available, which causes low internal quantum efficiency [6,7]. In contrast, despite the fact that phosphorescent OLEDs can take full advantage of excitons by doping iridium or platinum complexes, their presence brings high costs and environmental pollution [8,9]. In 2012, Adachi's team realized 100% internal quantum efficiency using TADF OLEDs [10]. TADF is the phenomenon of converting triplet excitons to singlet states via a fast RISC process under thermal activation [11,12]. Indeed, the luminous efficiency of molecules with the TADF properties suffer from the self-absorption effect, which hampers the efficiency improvement and affects practical application [13]. It is worth noting that the organic molecules with excited-state intramolecular proton transfer (ESIPT) properties can avoid this problem due to the significant Stokes shift [14–18]. ESIPT can be regarded as an ultrafast photo-tautomerization process in which a proton is transferred from proton donor to proton acceptor along with a strong intramolecular hydrogen bond (IHB) [19–23]. Therefore, the research of the organic TADF molecules capable of ESIPT effectively facilitates internal quantum efficiency, characterized by high luminous efficiency, low cost and long lifetime [24,25].

Additionally, 2,2′-bipyridine-3,3′-diol (BP(OH)$_2$) is a typical molecule that simultaneously exhibits the ESIPT properties and TADF features. Bulska et al. reported that BP(OH)$_2$ under the S$_1$ state would undergo a cooperative double ESIPT reaction [26]. Based on the double ESIPT form, Tokumura et al. put forward the TADF mechanism for BP(OH)$_2$ in hexane [27]. Concretely, after photoexcitation, the rapid double ESIPT happens, and then the T$_2$ structure can be obtained through the intersystem crossing (ISC) process in competition with emissions from the S$_1$ state. Following the ISC process, the reverse intersystem crossing (RISC) process from T$_2$ to S$_1$ state occurs, which thereby results in the TADF phenomenon. It was found that only the S$_1$ and T$_2$ states participate in the ISC and RISC processes. Plasser et al. deemed that BP(OH)$_2$ prefers to occur in the stepwise double ESIPT process rather than in the concerted double ESIPT process, based on the TDDFT and resolution-of-identity second-order approximate coupled-cluster methods [28]. Recently, Zhao et al. suggested that, in low-polar solvents, the single ESIPT is more likely to occur in BP(OH)$_2$ [29]. Accordingly, whether the molecule undergoes single or double proton transfer has not been identified completely. However, different geometric structures of the S$_1$ state significantly affect the spin-orbit coupling interaction between the singlet and triplet states, which further brings different TADF mechanisms [30,31]. Therefore, the previously proposed TADF mechanism based on the double ESIPT structure needs to be reconsidered.

In this study, we have demonstrated the ESIPT pathway and reconsidered the TADF mechanism of BP(OH)$_2$ theoretically in low-polar hexane solvent on account of density functional theory (DFT) and time-dependent density functional theory (TDDFT) methods. Specifically, the optimized geometric structures and absorption and emission peaks were analyzed to investigate the excited-state behavior for BP(OH)$_2$. In addition, the calculations of the frontier molecular orbitals (FMOs), infrared (IR) spectra, reduced density gradient (RDG), potential energy curves (PECs), potential energy surface (PES), and excited-state hydrogen-bond dynamics were applied to explore the ESIPT pathway. Moreover, the spin-orbit coupling (SOC) constants, energy level gaps and nonradiative decay rates were calculated to describe the TADF mechanism of BP(OH)$_2$. Furthermore, the electron-hole distribution was applied to analyze the electron excitation nature. In a word, our theoretical investigations demonstrate that BP(OH)$_2$ will undergo the single ESIPT process rather than the double ESIPT process, and provide reconsiderations of the mechanisms of the ISC and RISC processes involved in the TADF phenomenon of this molecule. These findings provide a theoretical foundation for understanding how the ESIPT mechanism affects TADF, which favors achieving highly efficient photoluminescence.

2. Results and Discussion

2.1. Structural Analysis and Absorption and Fluorescence Spectra

Figure 1 presents optimized geometric structures of S$_0$ and S$_1$ states for BP(OH)$_2$ in hexane at the B3LYP/def2-TZVP level with the dispersion correction (gd3bj). Meanwhile, the primary structural parameters involved in the IHBs of BP(OH)$_2$ in hexane are collected in Table 1. The optimized configurations show that the Enol* form for BP(OH)$_2$ does not exist in the S$_1$ state. In addition, there are two possible ESIPT pathways in the S$_1$ state: the single ESIPT path and double ESIPT path. For the single proton transfer path, the distance between N1 and H1 decreases from 1.659 Å to 1.026 Å, and that between O1 and H1 is elongated from 1.005 Å to 1.788 Å. For the double proton transfer path, the N1-H1 length is shortened from 1.659 Å to 1.034 Å, and O1-H1 is stretched from 1.005 Å to 1.725 Å. Similar to N1-H1 and O1-H1, the N2-H2 distance is decreased, while the length of O2–H2 exhibits a tendency of elongation. Therefore, the ESIPT pathways for BP(OH)$_2$ can be either the single ESIPT path or the double ESIPT path.
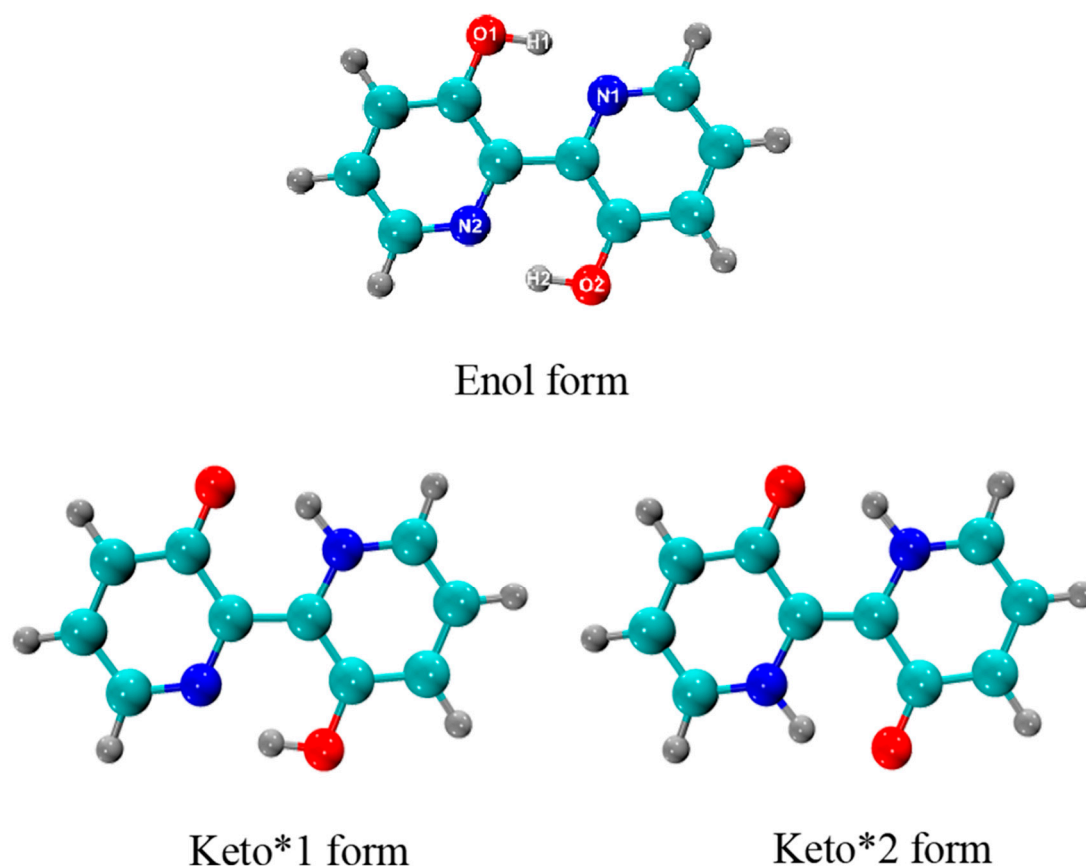
Figure 1. The optimized structure of BP(OH)$_2$ in the S$_0$ and S$_1$ states at the B3LYP/def2TZVP (gd3bj) IEFPCM (Hexane) level. Enol form: the initial conformation at the S$_0$ state; Keto*1 form: the conformation based on single ESIPT in the S$_1$ state; Keto*2 form: the conformation based on double ESIPT in the S$_1$ state. The blue atom represents N, the cyan atom represents C, the grey atom represents H, and red atom represents O.

Table 1. Obtained primary bond lengths for the optimized structure of BP(OH)$_2$ at the S$_0$ and S$_1$ states (Unit Å).

| Unit Å	Enol	Keto*1	Keto*2
N1-H1 (Å)	1.659	1.026	1.034
O1-H1 (Å)	1.005	1.788	1.725
N2-H2 (Å)	1.659	1.686	1.034
O2-H2 (Å)	1.000	1.000	1.724

The absorption and fluorescence peaks for BP(OH)$_2$ in hexane were calculated at the B3LYP/def2-TZVP (gd3bj) level. The relevant data are recorded in Table 2. The theoretical absorption maximum of the Enol form locates at 337 nm, being consistent with the experimental data (345 nm) [27]. This illustrates the dependability of our chosen calculation method for BP(OH)$_2$ system. The fluorescence peaks emitted from the optimized Keto*1 and Keto*2 forms are found at 484 nm and 479 nm, respectively, which coincide with the experimental peak (499 nm). Thus, the fluorescence is believed to be derived from the Keto*1 and Keto*2 structures combined with the optimized structures. However, in Table 2, the fluorescence peak of the Keto*1 conformation is in better agreement with 499 nm than that of the Keto*2 conformation.

Table 2. The absorption and emission peaks of BP(OH)$_2$ in hexane solvent.

	Abs. (nm)	Fluo. (nm)	
Exp.	345	499	
Theor.	337(Enol)	484(Keto*1)	479(Keto*2)

2.2. Frontier Molecular Orbitals

The tendency of the ESIPT behavior can be effectively affected by charge distribution changes [32]. For exploring the mechanism of the ESIPT process, we analyzed the charge distribution for the FMOs (HOMO and LUMO) of the S$_0$ and S$_1$ states in BP(OH)$_2$, as drawn in Figure 2. We find that the transition from HOMO to LUMO is corresponding to a dominant π-$\pi*$ type character, which plays a significant role in promoting the proton transfer. Herein, we focus only on the charge distribution around the IHB, affecting the excited-state hydrogen bond dynamics. As detailed in Figure 2, the electron density distribution of both hydroxyl oxygens, which are related to the ESIPT process, decreases, whereas that of the proton acceptors increases from HOMO to LUMO. These changes mean that the electronegativities of the nitrogen atoms are stronger than those of the oxygen atoms for BP(OH)$_2$ after the transition from HOMO to LUMO. Therefore, the FMOs analysis illustrates that both IHBs in BP(OH)$_2$ are reinforced upon excitation to S$_1$, which in turn facilitates the occurrence of the proton transfer process.

HOMO   LUMO
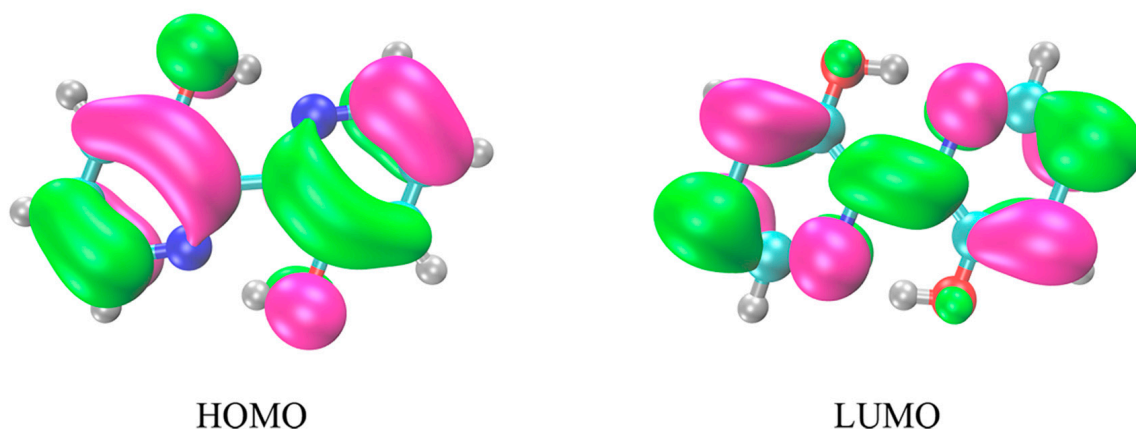
Figure 2. The HOMO and LUMO of BP(OH)$_2$ in hexane solvent.

2.3. Reduced Density Gradient Analysis

RDG can clearly characterize the interactions of molecules in real space and the intensity of the interactions [15,33]. Specifically, RDG can be expressed as the following Formula (1):

$$\mathrm{RDG(r)} = \frac{1}{2(3\pi^2)^{1/3}} \frac{|\nabla\rho(\mathrm{r})|}{\rho(\mathrm{r})^{4/3}} \tag{1}$$

In addition, the electron density $\rho(\mathrm{r})$ is associated with the eigenvalues I$_2$ in the Hessian matrix of electron density, as shown in Equation (2)

$$\Omega(\mathrm{r}) = \mathrm{sign}(\mathrm{I}_2(\mathrm{r}))\rho(\mathrm{r}) \tag{2}$$

Herein, the $\Omega(\mathrm{r}) < 0$ exhibits hydrogen-bonding interactions. The $\Omega(\mathrm{r}) \approx 0$ stands for the van der Waals interaction. The $\Omega(\mathrm{r}) > 0$ refers to the steric effect.

As for BP(OH)$_2$, to unveil the location and strength of IHB interactions and further judge the ESIPT pathway, the RDG image and gradient isosurfaces of this molecule are provided in Figure 3. The spikes inside the circles denote the strength of the hydrogen bond. Additionally, there is a blue disk between the oxygen and hydrogen atoms, and the hydrogen and nitrogen atoms, corresponding to the spikes in the circles. As detailed

in Figure 3, the spike position around −0.06 for BP(OH)$_2$ reveals the hydrogen-bonding interactions of O2-H2 . . . N2 and O1-H1 . . . N1 at the S$_0$ state. For the Keto*1 state, the two spike peaks located around −0.06 and −0.04 are attributed to O1-H1 . . . N1 and O2 . . . H2-N2, respectively. The IHBs corresponding to the Keto*2 state are O2 . . . H2-N2 and O1 . . . H1-N1 with the spike peak of −0.05. During the process from the S$_0$ to Keto*1 state, the IHB changes; namely, the proton H1 is transferred to N1 atoms. Moreover, the peak position of O2-H2 . . . N2 shifted from −0.06 of the S$_0$ state to −0.04 of the Keto*1 state, implying that the intensity of IHB (O2-H2 . . . N2) is weakened. The change of two IHBs means that only single ESIPT reaction can occur in BP(OH)$_2$. During the process from the S$_0$ to the Keto*2 state, the hydrogen bond positions change from O1-H1 . . . N1 and O2 H2 . . . N2 to O1 . . . H1-N1 and O2 . . . H2-N2. However, the absolute spike peaks (0.04) of the Keto*2 state are smaller than that of the O1 . . . H1-N1 in the Keto*1 state (0.05). This indicates that the strength of the newly formed IHB after the single ESIPT process is significantly stronger than those of the two IHBs after the double ESIPT process. Therefore, these results confirm that the intramolecular single ESIPT reaction is more likely to occur than the double ESIPT reaction.
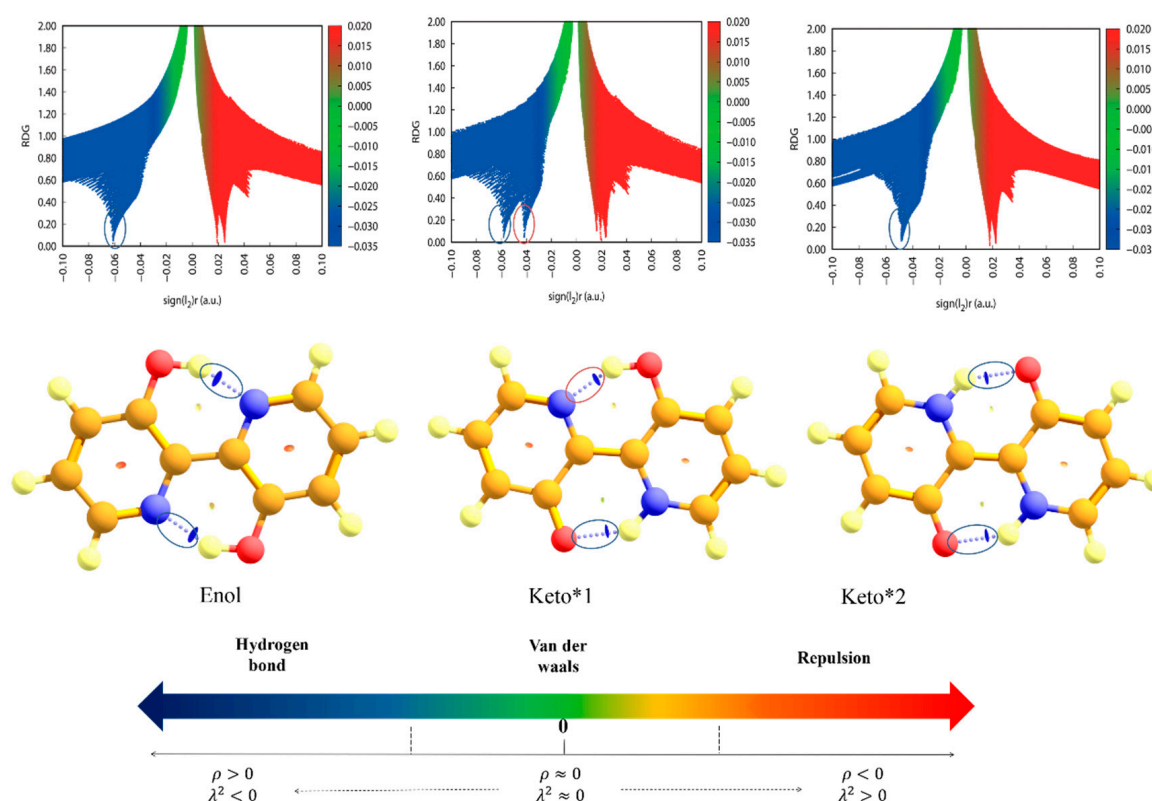

Figure 3. Diagrams of RDG (Function 1) vs. Ω(r) (Function 2) and gradient isosurfaces of BP(OH)$_2$ at Enol, Keto*1 and Keto*2 states.

2.4. Potential Energy Surface and Potential Energy Curves

In order to determine whether BP(OH)$_2$ takes place in the single or double proton transfer process, we constructed the PES of the S$_1$ state as a function of the bond lengths of O1-H1 and O2-H2. The PES is drawn in Figure 4a, where the black and red arrows represent the single ESIPT pathway and double ESIPT pathway, respectively. Importantly, the four stable points can be observed in Figure 4a. The PES of the S$_1$ state is symmetrical along the diagonal curve as a result of the symmetrical structure of BP(OH)$_2$. This means that BP(OH)$_2$ has three stable conformations in the S$_1$ state: the Enol* form, the Keto*1 form and the Keto*2 form. Specifically, in order to achieve the stable Keto*2 form, the double ESIPT pathway needs to surpass an energy barrier from the Enol* form to the Keto*2 form. However, there is no potential barrier in the single ESIPT pathway along

with O1-H1 . . . N1 or O2-H2 . . . N2. That is to say, the single ESIPT process will happen spontaneously when forming the Keto*1 conformation upon excitation to S_1. Consequently, the BP(OH)$_2$ in hexane will occur during the single ESIPT process instead of the double ESIPT, even though it possesses two IHBs.
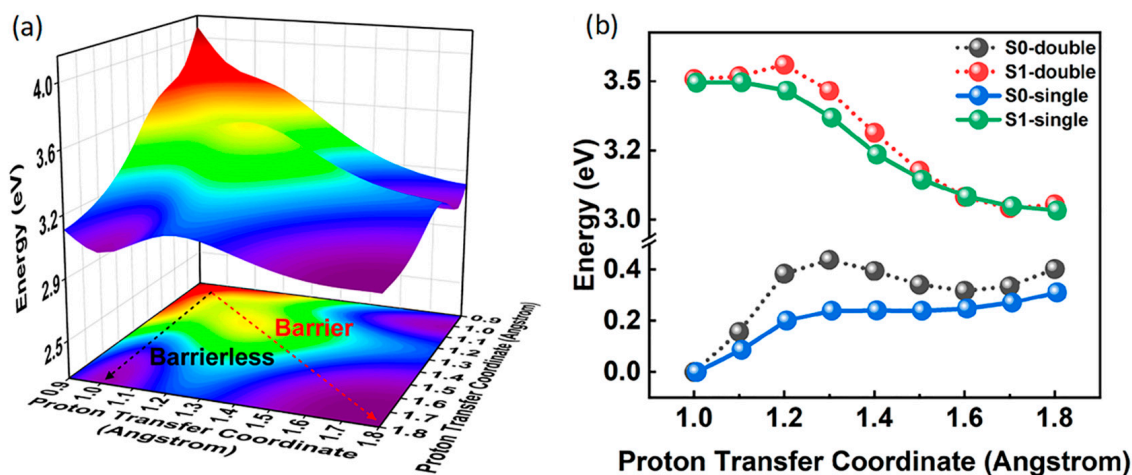

Figure 4. Constructed (**a**) PES in the S_1 state and (**b**) PECs in the S_0 and S_1 states for BP(OH)$_2$.

We further plotted the PECs in Figure 4b to compare the difference between the double and single proton transfer pathways clearly. The S_0 single curve shows that BP(OH)$_2$ exists in the Enol configuration in the S_0 state. For the S_0 double path, the high energy barrier prevents the double proton transfer behavior from taking place. These results mean that neither the single nor double proton transfer process can occur in the S_0 state. In addition, we notice that, for the S_1 double path, BP(OH)$_2$ needs to undergo an energy barrier forming two new hydrogen bonds (N1-H1 and N2-H2), while for the S_1 single path, there is only one stable structure, and the coordinate of this stable configuration is 1.724 Å. In other words, the BP(OH)$_2$ will take place in a barrierless single proton transfer process. Thus, it can be further attested that the double ESIPT pathway is ruled out due to the existence of a potential barrier.

2.5. Infrared Spectra

IR spectra are found to be an invaluable tool to describe hydrogen-bonding dynamics processes by analyzing the changes in vibration frequency [34]. To affirm our viewpoint once again—that only the single ESIPT occurs in the S_1 state—Figure 5 presents IR spectra of BP(OH)$_2$ (scaling factor 0.959) in the S_0 and S_1 states. The calculated IR spectra range from 2600 cm^{-1} to 3400 cm^{-1}, which involve vibration peaks for O1-H1, O2-H2 and N1-H1 groups. Specifically, in the S_0 state, there is only a characteristic peak around 2869 cm^{-1} due to the structural symmetry of BP(OH)$_2$, assigned to the O1-H1 and O2-H2 stretching vibration. When excited to S_1, the O2-H2 and N1-H1 stretching vibrational frequency of BP(OH)$_2$ are at 2918 cm^{-1} and 3153 cm^{-1}, respectively. Obviously, the IR spectrum of the S_1 state for BP(OH)$_2$ is different from that of the S_0 state. The vibration peak of O2-H2 exhibits a blue shift from 2869 cm^{-1} of the S_0 state to 2918 cm^{-1} of the S_1 state. This reveals that, following excitation to S_1, the IHB (O2-H2 . . . N2) is weakened, which is not conducive to the transfer of H2 protons. Interestingly, the O1-H1 vibration peak (2869 cm^{-1}) disappears in the S_1 state while the new N1-H1 peak (3153 cm^{-1}) forms, indicating the transfer of proton H1 from O1 to N1. Consequently, these results above demonstrate the occurrence of the single proton transfer process upon excitation.
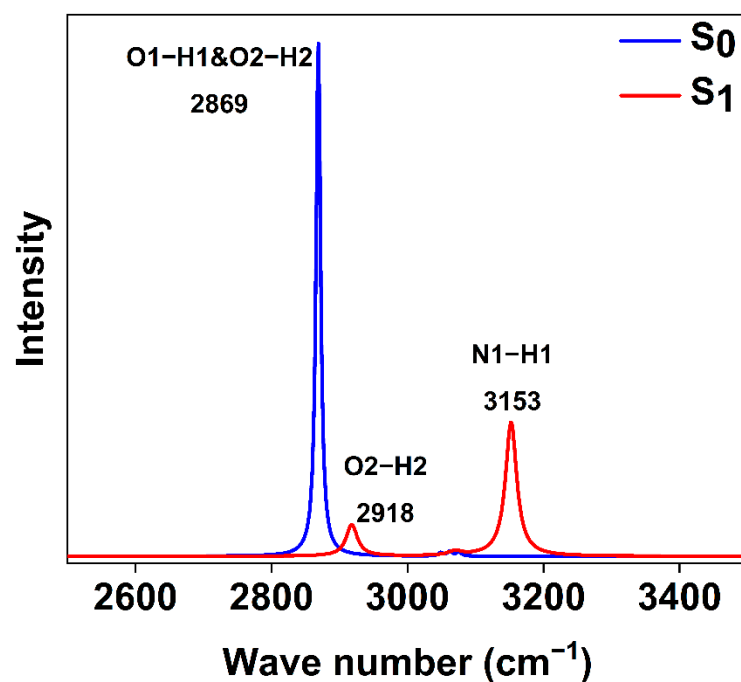
Figure 5. Calculated S_0 state and S_1 state infrared spectrum based on the single ESIPT structure of BP(OH)$_2$ in hexane.

2.6. Excited State Hydrogen Bond Dynamics

Considering that the timescale and characteristics of the ESIPT process may well be theoretically simulated and further revealed by excited-state hydrogen-bonding dynamics [35], the time-evolution trajectories of all bond lengths involved in IHBs are presented in Figure 6a. The Enol* form is the initial photoexcited configuration. In addition, at ~15 fs, the bond length of O1-H1 increases gradually with the time evolution, and the H1-N1 decreases gradually with the time evolution in comparison with the bond lengths of the Enol* form. These changes are due to the fact that the proton H1 moves along with a hydrogen bond from O1 to N1 rapidly until the proton H1 is transferred. After 15 fs, all the bond lengths related to the intramolecular hydrogen bond tend toward dynamic equilibrium. The Keto*1 form after 15 fs can be seen in Figure 6a. By comparing the Enol* form with the Keto*1 form, only the single ESIPT takes place in BP(OH)$_2$ upon excitation to the S_1 state.
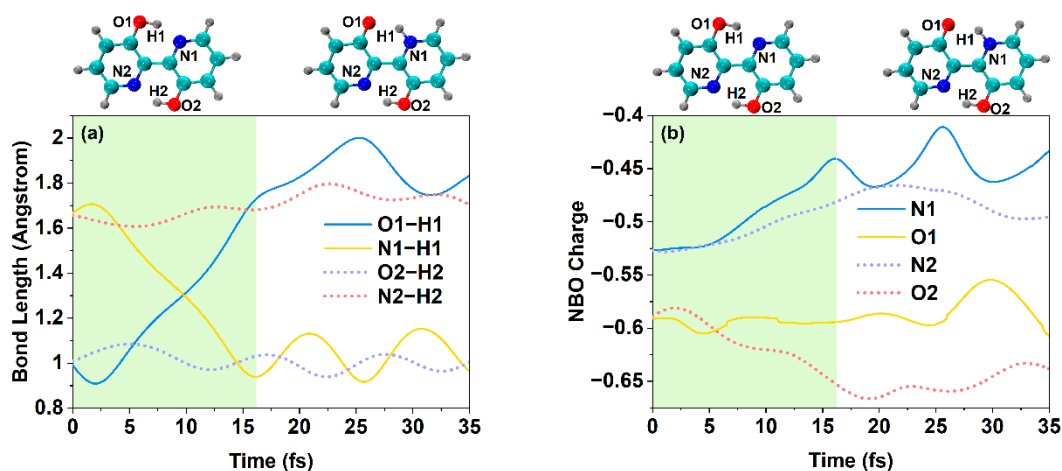

Figure 6. (**a**) The important bond lengths with time evolution, including the Enol* form (left) and Keto*1 form (right) and (**b**) the NBO charge of primary atoms with time evolution for BP(OH)$_2$, including the Enol* form (left) and Keto*1 form (right). Atoms of different colors in the Enol* and Keto* are represented as in Figure 1.

Due to the intramolecular charge redistribution having momentous effects on the ESIPT behavior, we also calculated the time evolution of the NBO charge for the atoms related to the proton transfer displayed in Figure 6b. For O1-H1 . . . N1, within 15 fs, the negative charge of the N1 atom decreases, while the electronegativity of O1 hardly obviously changes with time evolution. This phenomenon is due to the fact that the positively charged proton H1 gradually moves away from O1 to the N1 atom, which offsets the negative charge on N1. At the same time, the electronegativity of O2 increases gradually with time evolution, but the negative charge of N2 decreases with time evolution. These changes mean that the interaction between O2 and H2 is enhanced and the interaction between N2 and H2 atoms is weakened within 15 fs. Thus, it is not possible to transfer the proton H2 from O2 to N2. The NBO charge of all atoms related to the intramolecular hydrogen bond tends toward dynamic equilibrium after 15 fs. Based on the above analysis, the variety of the NBO charge once again supports the viewpoint that the $BP(OH)_2$ molecule will carry out the single proton transfer reaction instead of the double proton transfer upon excitation.

2.7. Spin-Orbit Coupling Interaction

The $BP(OH)_2$ molecule was found to exhibit not only single proton transfer properties but also the TADF phenomenon [27]. TADF phenomenon is closely correlated with the ISC and RISC processes. According to Fermi's golden rule [36], the larger SOC constant and the smaller energy level gap can promote the ISC and RISC processes. Therefore, to verify which triplet states are involved in the ISC process and elucidate the mechanism of the delayed fluorescence phenomenon, the energy level gaps and SOC constants are recorded in Table 3. To be specific, the energy level gaps for S_1-T_1, S_1-T_2 and S_1-T_3 are 0.980 eV, 0.120 eV and -0.046 eV, respectively. The energy level gaps of S_1-T_3 and S_1-T_2 are smaller than that of S_1-T_1, which makes the T_1 state difficult to induce the RISC process from T_1 to S_1. Based on that, the SOC_{ISC} constants of S_1-T_3 and S_1-T_2 are 31.029 cm^{-1} and 0.411 cm^{-1}. Obviously, the SOC_{ISC} constant of S_1-T_3 is much larger than that of S_1-T_2. Thus, the energy level gap, combined with spin-orbit coupling interaction, confirms that the ISC process is mainly the transition from the S_1 to the T_3 state. Correspondingly, it can be found that the SOC_{RISC} constants of S_1-T_1, S_1-T_2 and S_1-T_3 are 0.095 cm^{-1}, 0.585 cm^{-1} and 0.321 cm^{-1}, respectively. The SOC_{RISC} constants of S_1-T_3 and S_1-T_2 are larger than those of T_1-S_1, implying that the RISC process of T_2-S_1 and T_3-S_1 would be realized facilely.

Table 3. Calculated SOC constants, energy level difference and rates of ISC (K_{ISC}) and RISC (K_{RISC}) between the singlet and triplet states of $BP(OH)_2$ in hexane.

|	S_1-T_1	S_1-T_2	S_1-T_3
ΔE (eV)	0.980	0.120	-0.046
SOC_{ISC} (cm^{-1})	0.152	0.411	31.029
SOC_{RISC} (cm^{-1})	0.095	0.585	0.321
K_{ISC} (s^{-1})	1.40×10^6	1.73×10^6	1.05×10^{10}
K_{RISC} (s^{-1})	5.48×10^5	3.52×10^6	1.12×10^6

Since differences in the electron-hole distribution between the singlet and triplet states will affect the ISC process [37], we calculated the electron-hole distribution diagrams of the singlet (S_1 Keto*1) and triplet (T_2 Keto*1 and T_3 Keto*1) states, as plotted in Figure 7. In accordance with the El-Sayed rule [38], the transition between identical vibrational states is forbidden. Although the S_1, T_2 and T_3 states are characteristic of charge transfer, the electron-hole distribution of the S_1 state is different from that of T_2 and T_3 states. This means that there are two ISC transition channels, which are from the S_1 state to T_2 and from the S_1 state to T_3. During the excitation process, the T_3 state undergoes significant electron transfer and drastic alternation of electron distribution structure. In other words, the electron transfer from the S_1 state to T_3 is more pronounced than that from the S_1 state to T_2, which is the reason for the large SOC_{ISC} value between the S_1 and T_3 states. However, the degree of electron transfer in the S_1 state is close to that in the T_2 state, leading to a

smaller SOC_{ISC} value compared with SOC_{ISC} of the S_1 and T_3 states. Meanwhile, we find from Table 3 that the T_2 energy level is rather close to the T_3 energy level, which means that there may be an internal conversion process from the T_3 state to T_2. Thus, it is demonstrated that the T_3 energy level plays a significant role in collecting triplet state excitons.
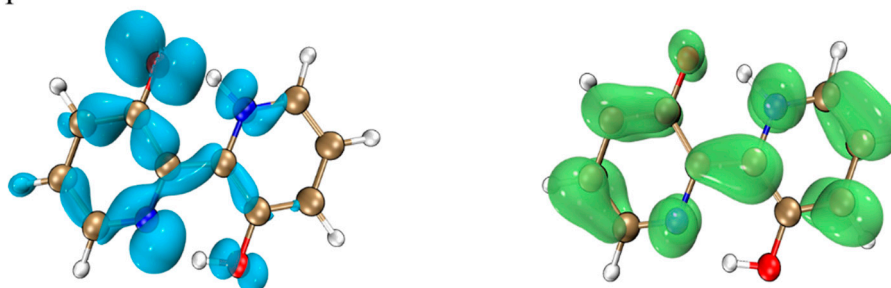
S_1 Keto*1
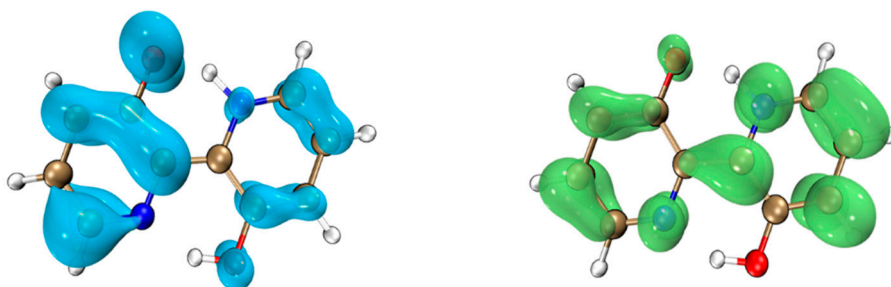
T_2 Keto*1
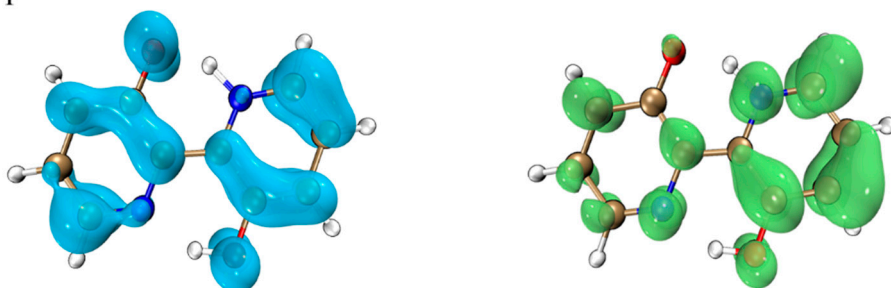
T_3 Keto*1

Figure 7. Electron-hole distribution based on the Keto*1 form in the excited states for $BP(OH)_2$. Blue color and green color represent holes and electrons, respectively. The golden atom represents C, the blue atom represents N, the red atom represents O, and light grey atom represents H.

For a more in-depth discussion of the ISC and RISC processes associated with TADF, the ISC and RISC rates of $BP(OH)_2$ in hexane are listed in Table 3. The ISC rates of S_1-T_1, S_1-T_2 and S_1-T_3 were calculated to be 1.40×10^6 s^{-1}, 1.73×10^6 s^{-1} and 1.05×10^{10} s^{-1}, respectively. The ISC rate of S_1-T_3 is four orders of magnitude larger than that of S_1-T_1 and S_1-T_2 due to the small energy level gap and the large SOC constant. Consequently, the result demonstrates that the ISC process will primarily happen from the S_1 state to T_3. Furthermore, the RISC rates of S_1-T_2 and S_1-T_3 are 3.52×10^6 s^{-1} and 1.12×10^6 s^{-1}, which are one order of magnitude larger than that of S_1-T_1. Thus, it is confirmed once again that the RISC process belongs to the transition from the T_3 state to S_1 and the one from the T_2 state to S_1. Through the above analysis, our calculated results illustrate that the ISC process is mainly assigned to the transition from the S_1 state to T_3, and the RISC process in $BP(OH)_2$ belongs to the transition from the T_3 state to S_1 and the one from the T_2 state to S_1. In the previous paper of Tokumura et al. [27], for $BP(OH)_2$, the ISC and RISC processes after the double proton transfer are the transition between the S_1 and T_2 states.

In contrast, herein, we reconsider the two processes based on the single proton transfer structure (Keto*1 form).

2.8. TADF Mechanism

Based on the analysis above, we describe the photophysical processes that give rise to the TADF phenomenon in BP(OH)$_2$, with the ESIPT feature displayed in Figure 8. Upon excitation to the S$_1$ state, BP(OH)$_2$ occurs in the intramolecular single proton transfer, forming the S$_1$ Keto*1 structure. Subsequently, the normal emission from the S$_1$ Keto*1 conformation occurs in competition with the efficient ISC process from the S$_1$ Keto*1 state to T$_3$ Keto*1. Following the ISC process, there are two possible RISC pathways: the transition from the T$_3$ Keto*1 state to S$_1$ Keto*1 and the one from the T$_2$ Keto*1 state to S$_1$ Keto*1. The BP(OH)$_2$ molecule that returns to the S$_1$ Keto*1 state decays to the S$_0$ Keto state by emitting delayed fluorescence. In summary, the luminescence is derived from the single ESIPT structure, and the T$_3$ state plays a crucial role in the TADF process due to the large electron-hole separation.
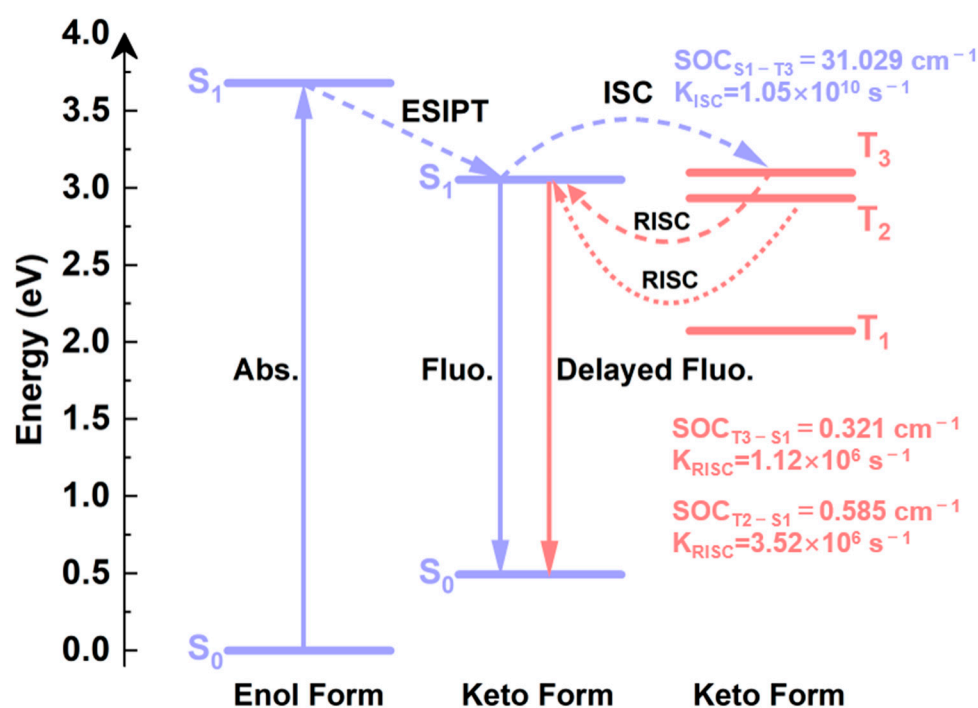

Figure 8. The schematic diagram of photoluminescence processes for BP(OH)$_2$ in hexane solvent.

3. Materials and Methods

All calculations in our work were completed using the DFT and TDDFT methods at the B3LYP/def2-TZVP level with the dispersion correction (gd3bj) [39–44]. The effect of the hexane solvent was considered with the integral equation formalism variant of the polarizable continuum model [45]. In this way, the optimized geometric structures, absorption and emission properties, FMOs, IR spectra, PECs, PES and excited-state hydrogen-bond dynamics were calculated in the Gaussian 16 package [46]. Vibrational frequencies were computed by determining the second derivatives of the energy with respect to the Cartesian nuclear coordinates and then transforming to mass-weighted coordinates. Concerning the ab initio molecular dynamics study of ESIPT, the classical trajectory calculation (i.e., Born–Oppenheimer molecular dynamics (BOMD)) was undertaken in the S$_1$ state [47,48]. The RDG image and the electron-hole distribution of the singlet and triplet states were analyzed using Multiwfn software [49]. In addition, the PySOC program interfaced with Gaussian 16 software was used to calculate the SOC constants [50,51]. Moreover, the nonradiative decay rates between singlet and triplet states were investigated in MOMAP [52–55].

4. Conclusions

The ESIPT-based TADF mechanisms of $BP(OH)_2$ were theoretically reconsidered at the B3LYP/def-2TZVP (gd3bj) level. Geometric structure, RDG scatter plots, PES and IR spectra indicate that $BP(OH)_2$ in hexane will undergo the single ESIPT process rather than the double ESIPT upon excitation to S_1 state. Furthermore, the BOMD computations prove once again the occurrence of the single ESIPT process and further provide the timescale for this process. Moreover, the energy level gaps, SOC constants and nonradiative decay rates of S_1-T_2, S_1-T_2 and S_1-T_2 were calculated based on the single ESIPT structure (Keto*1 form). These results elucidate that the ISC process is mainly the transition from the S_1 Keto*1 state to T_3 Keto*1, and the RISC process belongs to the transition from the T_3 Keto*1 state to S_1 Keto*1 and the one from the T_2 Keto*1 state to S_1 Keto*1. Furthermore, we find that the different electron-hole distributions between the singlet and triplet states of $BP(OH)_2$ facilitate the ISC process utilizing the electron-hole analysis. Thus, the T_3 state plays a dominant role in the TADF process, which is induced by the significant electron-hole separation between S_1 and T_3 states. Our work will not only be helpful to further understand the interaction between ESIPT and TADF but also contribute to achieving high luminescence efficiency for organic molecules with TADF properties.

Author Contributions: Data curation, X.Z.; Formal analysis, X.Z. and Q.L.; Funding acquisition, H.Y. and Y.S.; Methodology, H.Y.; Software, X.Z. and L.Z.; Supervision, H.Y. and Y.S.; Validation, H.Y.; Writing—original draft, X.Z.; Writing—review and editing, H.Y. and Y.S. All authors have read and agreed to the published version of the manuscript.

Institutional Review Board Statement: Not applicable.

Informed Consent Statement: Not applicable.

Data Availability Statement: Not applicable.

Conflicts of Interest: The authors declare that they have no known competing financial interest.

References

1. Vazquez, R.J.; Yun, J.H.; Muthike, A.K.; Howell, M.; Kim, H.; Madu, I.K.; Kim, T.; Zimmerman, P.; Lee, J.Y.; Iii, T.G. New Direct Approach for Determining the Reverse Intersystem Crossing Rate in Organic Thermally Activated Delayed Fluorescent (TADF) Emitters. *J. Am. Chem. Soc.* **2020**, *142*, 8074–8079. [CrossRef]
2. Bryden, M.A.; Zysman-Colman, E. Organic thermally activated delayed fluorescence (TADF) compounds used in photocatalysis. *Chem. Soc. Rev.* **2021**, *50*, 7587–7680. [CrossRef] [PubMed]
3. Chen, X.K.; Kim, D.; Bredas, J.L. Thermally Activated Delayed Fluorescence (TADF) Path toward Efficient Electroluminescence in Purely Organic Materials: Molecular Level Insight. *Acc. Chem. Res.* **2018**, *51*, 2215–2224. [CrossRef] [PubMed]
4. Gibson, J.; Penfold, T.J. Nonadiabatic coupling reduces the activation energy in thermally activated delayed fluorescence. *Phys. Chem. Chem. Phys.* **2017**, *19*, 8428–8434. [CrossRef] [PubMed]
5. Sheng, R.; Yang, L.; Li, A.; Chen, K.; Zhang, F.; Duan, Y.; Zhao, Y.; Chen, P. Highly efficient orange and white OLEDs based on ultrathin phosphorescent emitters with double reverse intersystem crossing system. *J. Lumin.* **2022**, *246*, 118852. [CrossRef]
6. Liu, H.; Liu, Z.; Li, G.; Huang, H.; Zhou, C.; Wang, Z.; Yang, C. Versatile Direct Cyclization Constructs Spiro-acridan Derivatives for Highly Efficient TADF emitters. *Angew. Chem. Int. Ed.* **2021**, *60*, 12376–12380. [CrossRef]
7. Fan, J.; Zhang, Y.; Zhou, Y.; Lin, L.; Wang, C.-K. Excited State Properties of a Thermally Activated Delayed Fluorescence Molecule in Solid Phase Studied by Quantum Mechanics/Molecular Mechanics Method. *J. Phys. Chem. C* **2018**, *122*, 2358–2366. [CrossRef]
8. Hu, Y.-Y.; Luo, W.; Hu, C.-G.; Wang, Y.; Tong, B.-H.; Fung, M.-K.; Tian, Y.-P.; Zhang, Q.-F. The one-pot synthesis of homoleptic phenylphthalazine iridium(III) complexes and their application in high efficiency OLEDs. *J. Lumin.* **2020**, *219*, 116846. [CrossRef]
9. Fan, J.; Zhang, Y.; Ma, Y.; Song, Y.; Lin, L.; Xu, Y.; Wang, C.-K. The role of intermolecular interactions in regulating the thermally activated delayed fluorescence and charge transfer properties: A theoretical perspective. *J. Mater. Chem. C* **2020**, *8*, 8601–8612. [CrossRef]
10. Lin, L.; Wang, Z.; Fan, J.; Wang, C. Theoretical insights on the electroluminescent mechanism of thermally activated delayed fluorescence emitters. *Org. Electron.* **2017**, *41*, 17–25. [CrossRef]
11. Dos Santos, P.L.; Etherington, M.K.; Monkman, A.P. Chemical and conformational control of the energy gaps involved in the thermally activated delayed fluorescence mechanism. *J. Mater. Chem. C* **2018**, *6*, 4842–4853. [CrossRef]

12. Zhou, D.; Liu, D.; Gong, X.; Ma, H.; Qian, G.; Gong, S.; Xie, G.; Zhu, W.; Wang, Y. Solution-Processed Highly Efficient Bluish-Green Thermally Activated Delayed Fluorescence Emitter Bearing an Asymmetric Oxadiazole-Difluoroboron Double Acceptor. *ACS Appl. Mater. Interfaces* **2019**, *11*, 24339–24348. [CrossRef] [PubMed]

13. Azarias, C.; Budzak, S.; Laurent, A.D.; Ulrich, G.; Jacquemin, D. Tuning ESIPT fluorophores into dual emitters. *Chem. Sci.* **2016**, *7*, 3763–3774. [CrossRef] [PubMed]

14. Li, Y.; Sun, C.; Han, J.; Zhou, Q.; Cao, B.; Yin, H.; Shi, Y. Theoretical investigation of intermolecular hydrogen bond induces fluorescence quenching phenomenon for Coumarin-1. *J. Lumin.* **2020**, *221*, 117110. [CrossRef]

15. Sun, C.; Zhang, X.; Diao, L.; Cao, B.; Yin, H.; Shi, Y. How the atomic electron-accepting ability affect the double ESIPT process of 2,5-bis(benzoxazol-2-yl)thiophene-3,4-diol? *J. Lumin.* **2020**, *225*, 117329. [CrossRef]

16. Yin, H.; Zhang, Y.-M.; Zhao, H.-F.; Yang, G.; Shi, Y.; Zhang, S.X.-A.; Ding, D.-J. Optical anti-counterfeiting of a single molecule by two solvents based on intra- and intermocular excited state proton transfer mechanisms. *Dyes Pigments* **2018**, *159*, 506–512. [CrossRef]

17. Zhao, J.; Dong, H.; Zheng, Y. Elaborating the excited state multiple proton transfer mechanism for 9Hpyrido[3,4-b]indole. *J. Lumin.* **2018**, *195*, 228–233. [CrossRef]

18. Zhu, L.; Zhou, Q.; Cao, B.; Li, B.; Wang, Z.; Zhang, X.; Yin, H.; Shi, Y. Theoretical reconsideration of the mechanism of the excited state proton transfer of indigo carmine in water. *J. Mol. Liq.* **2022**, *347*, 118365. [CrossRef]

19. Yang, Y.; Zhao, J.; Li, Y. Theoretical Study of the ESIPT Process for a New Natural Product Quercetin. *Sci. Rep.* **2016**, *6*, 32152. [CrossRef]

20. Song, P.; Ma, F.-C. Intermolecular hydrogen-bonding effects on photophysics and photochemistry. *Int. Rev. Phys. Chem.* **2013**, *32*, 589–609. [CrossRef]

21. Yin, H.; Shi, Y.; Wang, Y. Time-dependent density functional theory study on the excited-state intramolecular proton transfer in salicylaldehyde. *Spectrochim. Acta A Mol. Biomol. Spectrosc.* **2014**, *129*, 280–284. [CrossRef] [PubMed]

22. Sun, L.; Chen, Y.; Sun, M. Exploring Nonemissive Excited-State Intramolecular Proton Transfer by Plasmon-Enhanced Hyper-Raman Scattering and Two-Photon Excitation Fluorescence. *J. Phys. Chem. C* **2021**, *126*, 487–492. [CrossRef]

23. Yang, Y.; Zhang, Q.; Liu, Y.; Jiang, Z.; Qin, C.; Jiang, K.; Liu, Y. Ultrafast dynamics of dual fluorescence of 2-(2′-hydroxyphenyl) benzothiazole and its derivatives by femtosecond transient absorption spectroscopy. *J. Lumin.* **2022**, *248*, 118922. [CrossRef]

24. Cao, Y.; Eng, J.; Penfold, T.J. Excited State Intramolecular Proton Transfer Dynamics for Triplet Harvesting in Organic Molecules. *J. Phys. Chem. A* **2019**, *123*, 2640–2649. [CrossRef] [PubMed]

25. Wu, K.; Zhang, T.; Wang, Z.; Wang, L.; Zhan, L.; Gong, S.; Zhong, C.; Lu, Z.H.; Zhang, S.; Yang, C. De Novo Design of Excited-State Intramolecular Proton Transfer Emitters via a Thermally Activated Delayed Fluorescence Channel. *J. Am. Chem. Soc.* **2018**, *140*, 8877–8886. [CrossRef] [PubMed]

26. Bulska, H. Intramolecular cooperative double proton transfer in [2,2′-bipyridyl]-3,3′-diol. *Chem. Phys. Lett.* **1983**, *98*, 398–402. [CrossRef]

27. Kunihiro, T.; Mutsuo, K.; Osamu, O. Reverse intersystem crossing from higher triplet to excited singlet in 2,2′-bipyridine-3,3′-diol phototautomer. *J. Photochem. Photobiol. A Chem.* **1994**, *81*, 151–158. [CrossRef]

28. Plasser, F.; Barbatti, M.; Aquino, A.J.A.; Lischka, H. Excited-state diproton transfer in [2,2′-bipyridyl]-3,3′-diol: The mechanism is sequential, not concerted. *J. Phys. Chem. A* **2009**, *113*, 8490–8499. [CrossRef]

29. Zhao, J.; Liu, X.; Zheng, Y. Controlling Excited State Single versus Double Proton Transfer for 2,2′-Bipyridyl-3,3′-diol: Solvent Effect. *J. Phys. Chem. A* **2017**, *121*, 4002–4008. [CrossRef]

30. Chen, K.; Kurganskii, I.V.; Zhang, X.; Elmali, A.; Zhao, J.; Karatay, A.; Fedin, M.V. Intersystem Crossing and Electron Spin Selectivity in Anthracene-Naphthalimide Compact Electron Donor-Acceptor Dyads Showing Different Geometry and Electronic Coupling Magnitudes. *Chem. Eur. J.* **2021**, *27*, 7572–7587. [CrossRef]

31. Xu, C.; Yu, L.; Zhu, C.; Yu, J.; Cao, Z. Intersystem crossing-branched excited-state intramolecular proton transfer for o-nitrophenol: An ab initio on-the-fly nonadiabatic molecular dynamic simulation. *Sci. Rep.* **2016**, *6*, 26768. [CrossRef] [PubMed]

32. Wang, W.; Marshall, M.; Collins, E.; Marquez, S.; Mu, C.; Bowen, K.H.; Zhang, X. Intramolecular electron-induced proton transfer and its correlation with excited-state intramolecular proton transfer. *Nat. Commun.* **2019**, *10*, 1170. [CrossRef] [PubMed]

33. Chen, J.; Yu, T.; Ubba, E.; Xie, Z.; Yang, Z.; Zhang, Y.; Liu, S.; Xu, J.; Aldred, M.P.; Chi, Z. Achieving Dual-Emissive and Time-Dependent Evolutive Organic Afterglow by Bridging Molecules with Weak Intermolecular Hydrogen Bonding. *Adv. Opt. Mater.* **2019**, *7*, 1801593. [CrossRef]

34. Samant, V.; Singh, A.K.; Ramakrishna, G.; Ghosh, H.N.; Ghanty, T.K.; Palit, D.K. Ultrafast Intermolecular Hydrogen Bond Dynamics in the Excited State of Fluorenone. *J. Phys. Chem. A* **2005**, *109*, 8693–8704. [CrossRef] [PubMed]

35. Dommett, M.; Crespo-Otero, R. Excited state proton transfer in 2′-hydroxychalcone derivatives. *Phys. Chem. Chem. Phys.* **2017**, *19*, 2409–2416. [CrossRef]

36. Lawetz, V.; Orlandi, G.; Siebrand, W. Theory of Intersystem Crossing in Aromatic Hydrocarbons. *J. Chem. Phys.* **1972**, *56*, 4058–4072. [CrossRef]

37. Jiang, G.; Li, F.; Fan, J.; Song, Y.; Wang, C.-K.; Lin, L. Theoretical perspective for luminescent mechanism of thermally activated delayed fluorescence emitter with excited-state intramolecular proton transfer. *J. Mater. Chem. C* **2020**, *8*, 98–108. [CrossRef]

38. Samanta, P.K.; Kim, D.; Coropceanu, V.; Bredas, J.L. Up-Conversion Intersystem Crossing Rates in Organic Emitters for Thermally Activated Delayed Fluorescence: Impact of the Nature of Singlet vs Triplet Excited States. *J. Am. Chem. Soc.* **2017**, *139*, 4042–4051. [CrossRef]

39. Zhang, M.; Ren, B.; Wang, Y.; Zhao, C. A DFT/TDDFT study on the excited-state hydrogen bonding dynamics of 6-aminocoumarin in water solution. *Spectrochim. Acta A Mol. Biomol. Spectrosc.* **2013**, *101*, 191–195. [CrossRef]

40. Grimme, S.; Antony, J.; Ehrlich, S.; Krieg, H. A consistent and accurate ab initio parametrization of density functional dispersion correction (DFT-D) for the 94 elements H-Pu. *J. Chem. Phys.* **2010**, *132*, 154104. [CrossRef]

41. Lanke, S.K.; Sekar, N. Pyrazole based NLOphores: Synthesis, photophysical, DFT, TDDFT studies. *Dyes Pigments* **2016**, *127*, 116–127. [CrossRef]

42. Salomon, O.; Reiher, M.; Hess, B.A. Assertion and validation of the performance of the B3LYP⋆ functional for the first transition metal row and the G2 test set. *J. Chem. Phys.* **2002**, *117*, 4729–4737. [CrossRef]

43. Navarro, L.; Rodriguez, F.; Cirera, J. Controlling the spin-crossover behavior of the [Cr(indenyl)2] family via ligand functionalization. *Dalton Trans.* **2021**, *50*, 8704–8710. [CrossRef] [PubMed]

44. Chrayteh, M.; Huet, T.R.; Drean, P. Microsolvation of myrtenal studied by microwave spectroscopy highlights the role of quasi-hydrogen bonds in the stabilization of its hydrates. *J. Chem. Phys.* **2020**, *153*, 104304. [CrossRef] [PubMed]

45. Mennucci, B.; Cancès, E.; Tomasi, J. Evaluation of Solvent Effects in Isotropic and Anisotropic Dielectrics and in Ionic Solutions with a Unified Integral Equation Method: Theoretical Bases, Computational Implementation, and Numerical Applications. *J. Phys. Chem. B* **1997**, *101*, 10506–10517. [CrossRef]

46. Frisch, M.J.; Trucks, G.W.; Schlegel, H.B.; Scuseria, G.E.; Robb, M.A.; Cheeseman, J.R.; Scalmani, G.; Barone, V.; Petersson, G.A.; Nakatsuji, H.; et al. *Gaussian 16, Revision B 01*; Gaussian, Inc.: Wallingford, CT, USA, 2016.

47. Nguyen, P.D.; Ding, F.; Fischer, S.A.; Liang, W.; Li, X. Solvated First-Principles Excited-State Charge-Transfer Dynamics with Time-Dependent Polarizable Continuum Model and Solvent Dielectric Relaxation. *J. Phys. Chem. Lett.* **2012**, *3*, 2898–2904. [CrossRef]

48. Yin, H.; Li, B.; Zhao, X.; Liu, Y.; Shi, Y.; Ding, D. Restriction of intramolecular torsion induces abnormal blue-shifted fluorescence in the aggregate state. *Dyes Pigments* **2022**, *201*, 110192. [CrossRef]

49. Lu, T.; Chen, F. Multiwfn: A multifunctional wavefunction analyzer. *J. Comput. Chem.* **2012**, *33*, 580–592. [CrossRef]

50. Gao, X.; Bai, S.; Fazzi, D.; Niehaus, T.; Barbatti, M.; Thiel, W. Evaluation of Spin-Orbit Couplings with Linear-Response Time-Dependent Density Functional Methods. *J. Chem. Theory Comput.* **2017**, *13*, 515–524. [CrossRef]

51. Li, Q.; Wan, Y.; Zhou, Q.; Li, Y.; Li, B.; Zhu, L.; Wan, Y.; Yin, H.; Shi, Y. Exploring the effect of nitrile substituent position on fluorescence quantum yield of ESIPT-based oxazoline derivatives: A TDDFT investigation. *Spectrochim. Acta A Mol. Biomol. Spectrosc.* **2022**, *272*, 120953–120959. [CrossRef]

52. Niu, Y.; Li, W.; Peng, Q.; Geng, H.; Yi, Y.; Wang, L.; Nan, G.; Wang, D.; Shuai, Z. MOlecular MAterials Property Prediction Package (MOMAP) 1.0: A software package for predicting the luminescent properties and mobility of organic functional materials. *Mol. Phys.* **2018**, *116*, 1078–1090. [CrossRef]

53. Peng, Q.; Yi, Y.; Shuai, Z.; Shao, J. Toward Quantitative Prediction of Molecular Fluorescence Quantum Efficiency: Role of Duschinsky Rotation. *J. Am. Chem. Soc.* **2007**, *129*, 9333–9339. [CrossRef] [PubMed]

54. Niu, Y.; Peng, Q.; Shuai, Z. Promoting-mode free formalism for excited state radiationless decay process with Duschinsky rotation effect. *Sci. China Chem.* **2008**, *51*, 1153–1158. [CrossRef]

55. Shuai, Z. Thermal Vibration Correlation Function Formalism for Molecular Excited State Decay Rates. *Chin. J. Chem.* **2020**, *38*, 1223–1232. [CrossRef]